BIOPHYSICS

Structures and an activation mechanism of human potassium-chloride cotransporters

Yuan Xie[1]*, Shenghai Chang[1,2]*, Cheng Zhao[1], Feng Wang[3], Si Liu[4], Jin Wang[5], Eric Delpire[6]†, Sheng Ye[4,7]†, Jiangtao Guo[1,8]†

Potassium-chloride cotransporters KCC1 to KCC4 mediate the coupled export of potassium and chloride across the plasma membrane and play important roles in cell volume regulation, auditory system function, and γ-aminobutyric acid (GABA) and glycine-mediated inhibitory neurotransmission. Here, we present 2.9- to 3.6-Å resolution structures of full-length human KCC2, KCC3, and KCC4. All three KCCs adopt a similar overall architecture, a domain-swap dimeric assembly, and an inward-facing conformation. The structural and functional studies reveal that one unexpected N-terminal peptide binds at the cytosolic facing cavity and locks KCC2 and KCC4 at an autoinhibition state. The C-terminal domain (CTD) directly interacts with the N-terminal inhibitory peptide, and the relative motions between the CTD and the transmembrane domain (TMD) suggest that CTD regulates KCCs' activities by adjusting the autoinhibitory effect. These structures provide the first glimpse of full-length structures of KCCs and an autoinhibition mechanism among the amino acid–polyamine-organocation transporter superfamily.

INTRODUCTION

Encoded by the Solute Carrier 12 (*SLC12*) gene family, the human cation-chloride cotransporters (CCCs) mediate coupled movement of Cl^- with K^+ and/or Na^+ across the plasma membrane and are critical for maintaining K^+, Na^+ and Cl^- homeostasis (*1*, *2*). CCCs can be divided into two major branches (*3*, *4*), the sodium-dependent cotransporters NKCC1 to NKCC2 and NCC (SLC12A1 to SLC12A3), and the sodium-independent cotransporters KCC1 to KCC4 (SLC12A4 to SLC12A7). NKCCs and NCC import Cl^- into the cell driven by the transmembrane Na^+ gradient, while KCCs export intracellular Cl^- using an energy stored in the K^+ electrochemical potential. CCCs transport electroneutral substrates across membrane, with stoichiometry of 1 K^+:1Cl^- for KCCs, 1Na^+:1Cl^- for the NCC, and 1 K^+:1Na^+:2Cl^- for NKCCs (*1*).

CCCs are widely expressed and found in tissues such as brain, kidney, intestine, lung, muscle, heart, etc. By modulating ionic homeostasis, CCCs contribute to a variety of physiological processes, such as salt reabsorption in kidney (*5*); salt secretion in lung, stomach (*6*, *7*), and intestine (*8*); auditory system function (*9*); cell volume regulation of erythrocytes (*10*) and other cells (*11*); and γ-aminobutyric acid and glycine-mediated inhibitory neurotransmission (*12*, *13*). Mutations in CCCs lead to various human diseases. Loss-of-function mutations in human NCC and NKCC2 result in salt-wasting disorders such as Gitelman syndrome and Bartter syndrome (*14*, *15*), whereas dysfunction of KCC3 causes Andermann syndrome or hereditary motor and sensory neuropathy with agenesis of the corpus callosum (HMSN/ACC), a rare neurodegenerative genetic disorder associated with various degrees of agenesis of the corpus callosum (*16*). Besides, mutations in KCC2 result in two types of human epilepsy, idiopathic generalized epilepsy (*17*), and epilepsy of infancy with migrating focal seizures (*18*, *19*). Therefore, CCCs are important drug targets for the treatment of hypertension, epilepsy, and other neurological diseases. The diuretics furosemide and thiazide have been clinically used as antihypertensive drugs by reducing the activity of NKCC2 and NCC, respectively (*20*, *21*). Using high-throughput screening assays, several groups have developed KCC-specific antagonists (*22*, *23*), as well as a KCC2-specific agonist CLP257 and its prodrug CLP290, which increase the plasma membrane expression of KCC2 and reduce intracellular Cl^- concentration in the animal model, making them potential drugs for the treatment of epilepsy (*24*–*26*).

The four KCCs share conserved structural features, including the amino acid–polyamine-organocation superfamily fold of the transmembrane domain (TMD), an extracellular domain (ECD) mainly formed by a large loop between transmembrane helix 5 (TM5) and TM6, and the C-terminal domain (CTD), which follows TM12 (*27*–*29*). The CTD regulates expression, trafficking (*30*, *31*), and activity of KCCs by phosphorylation and dephosphorylation (*32*–*34*). The modulation of CCCs activity by the CTD is further supported by the fluorescence resonance energy transfer (FRET) assays, which showed that the regulation of NKCC1 activity accompanies a large movement between the CTD dimer (*35*, *36*).

Previously, structures of NKCC1, KCC1, and KCC4 reveal the overall architecture, ion binding sites, and different oligomeric states of the CCC family (*37*–*40*), yet, the full-length structures of KCCs remain unknown. In addition, as the structures of human NKCC1 and KCC1 and mouse KCC4 all lose the CTDs, whether the dynamic feature of the CTD is functionally relevant awaits further study. In this study, we report full-length structures of human KCC2, KCC3, and KCC4, observe an autoinhibition by the N-terminal

[1]Department of Biophysics, and Department of Pathology of Sir Run Run Shaw Hospital, Zhejiang University School of Medicine, Hangzhou 310058, China. [2]Center of Cryo Electron Microscopy, Zhejiang University School of Medicine, Hangzhou 310058, China. [3]Wuxi Biortus Biosciences Co. Ltd., 6 Dongsheng West Road, Jiangyin, 214437, China. [4]Tianjin Key Laboratory of Function and Application of Biological Macromolecular Structures, School of Life Sciences, Tianjin University, 92 Weijin Road, Nankai District, Tianjin 300072, China. [5]Department of Pathology of Sir Run Run Shaw Hospital, Zhejiang University School of Medicine, Hangzhou 310058, China. [6]Department of Anesthesiology, Vanderbilt University School of Medicine, Nashville, TN 37232, USA. [7]Life Sciences Institute and Innovation Center for Cell Signaling Network, Zhejiang University, Hangzhou, Zhejiang 310058, China. [8]Department of Cardiology, Key Laboratory of Cardiovascular Intervention and Regenerative Medicine of Zhejiang Province, Sir Run Run Shaw Hospital, Zhejiang University School of Medicine, Hangzhou, 310016, China.
*These authors contributed equally to this work.
†Corresponding author. Email: jiangtaoguo@zju.edu.cn (J.G.); sye@tju.edu.cn (S.Y.); eric.delpire@vanderbilt.edu (E.D.).

peptide, and reveal diverse dimeric assembly, which may be implicated in the regulation of the transporters' activity.

RESULTS AND DISCUSSIONS

Structure determination and overall structures of KCC2, KCC3, and KCC4

We determined electron cryo-microscopy (cryo-EM) structures of the full-length human KCC2a isoform at 3.4-Å resolution, KCC3a at 3.6-Å resolution, and KCC4a at 2.9-Å resolution (Fig. 1, A to C, figs. S1 to S3, and table S1). In all three maps, the ECDs, TMDs, and CTDs are well resolved, resulting in ~80% sequence coverage of the transporter for each model. In addition, the 3D classifications identified additional classes, one class of KCC2 with only the ECD/TMD (KCC2 class II, KCC2C2), one of KCC3 with the ECD/TMD and lower-quality CTD (KCC3 class II, KCC3C2), and one of KCC4 with only the CTD (KCC4 class II, KCC4C2; figs. S1 to S3). These three classes were refined to 5- to 8-Å resolutions. The higher-resolution KCC2, KCC3, and KCC4 share a similar overall architecture and dimerization assembly, with a root mean square (RMS) deviation of 0.97 Å over 877 Cα atoms within one subunit between KCC2 and KCC3 and 0.88 Å over 884 Cα atoms between KCC2 and KCC4. During the following discussion, unless otherwise mentioned, we will focus on the structure of KCC2.

In a KCC2 dimer, the twofold axes of the TMDs and CTDs coincide and are perpendicular to the membrane surface. The CTD from one subunit attaches to the TMD of the opposing subunit at the cytosolic surface of the membrane, displaying a domain-swap organization (Fig. 1A). The dimerization is mainly attributed to the extensive interactions between two CTDs, as well as the hydrophobic interactions mediated by TM11 and TM12 helices in the TMDs (Fig. 1A). The two ECDs are apart from each other by the shortest atom-to-atom distance of about 8 Å and not involved in the dimeric interactions.

As previously revealed by the KCC1 structure (*38*), KCC2 adopts a LeuT-like fold in the TMD, with an inverted repeat structure formed by TM1-5 and TM6-10 (Fig. 1D). All KCC2, KCC3, and KCC4 are in an inward facing conformation, and the intracellular facing cavity of KCC2 and KCC4 is occluded by a clearly resolved N-terminal peptide (Fig. 1E and fig. S4). The ECD, formed by the two ordered linkers between TM5-6 and TM7-8, sits on top of the extracellular surface of the TMD. The long TM5-6 linker maintains a relatively rigid architecture by two conserved disulfide bonds, two pairs of antiparallel β strands, several short α helices, and the glycosylation at multiple Asn residues (Fig. 1E). The TMD and the CTD are connected through TM12 and the scissor helix (Fig. 1E), which was first observed in the zebrafish NKCC1 structure (*39*).

The highly conserved TMD and ion binding sites among KCC family

KCC2 displays a very high structural similarity to KCC1 in the TMD region, with an RMS deviation of 0.74 Å over 396 Ca atoms (Fig. 2A). Superimposition of KCC2 onto KCC1 reveals that the first 11 transmembrane helices, including key residues for ions coordination, align well (Fig. 2B), indicating that KCC2 shares a similar substrate recognition and transport mechanism. Because of the resolution limit, we were unable to unambiguously assign K^+ or Cl^- ions in the KCC2 structure. TM12 in KCC2 adopts a different orientation and forms a ~20° angle with that of KCC1 (Fig. 2A). In KCC2, TM12 contacts TM3, TM10, and TM8-9 linker with hydrophobic

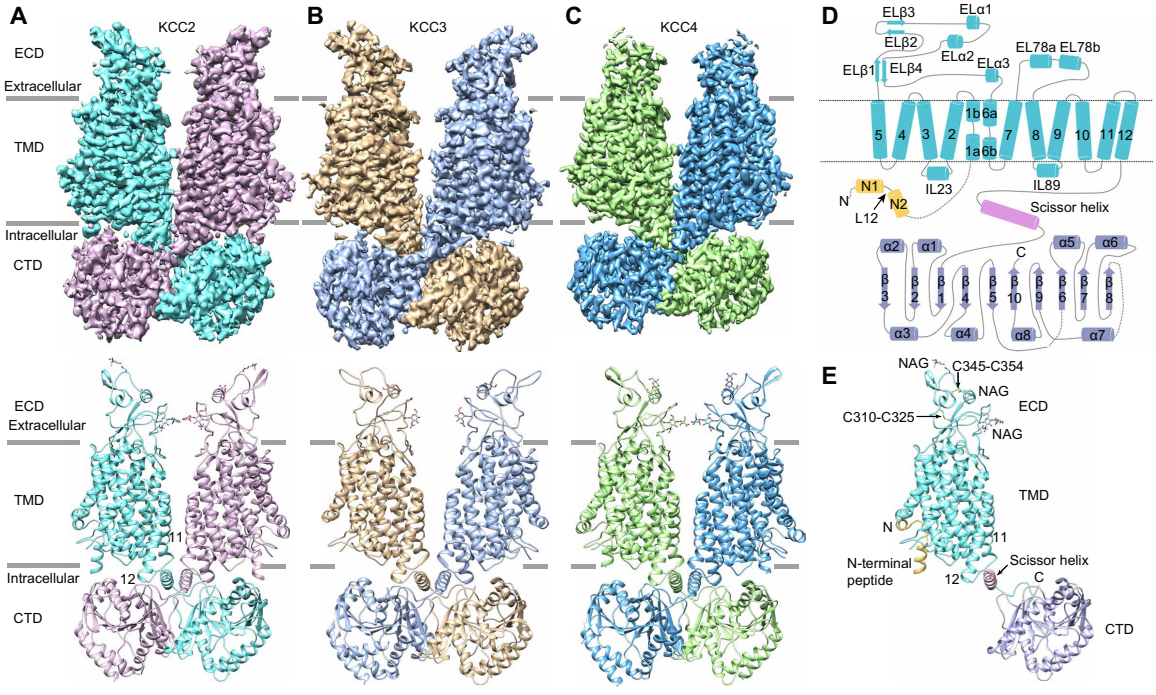

Fig. 1. Overall structures of human KCC2, KCC3, and KCC4. (**A** to **C**) Side views of three-dimensional reconstructions (upper) and cartoon representations (lower) of human KCC2 (A), KCC3 (B), and KCC4 (C), with each subunit colored individually. All *N*-acetylglucosamines (NAGs) are shown as sticks. The gray bars on either side of the structure define the position (top and bottom) of the cell membrane. (**D**) Topology arrangement of the KCC2. (**E**) Structure of one KCC2 subunit in side view. Each domain is colored the same as in (D).

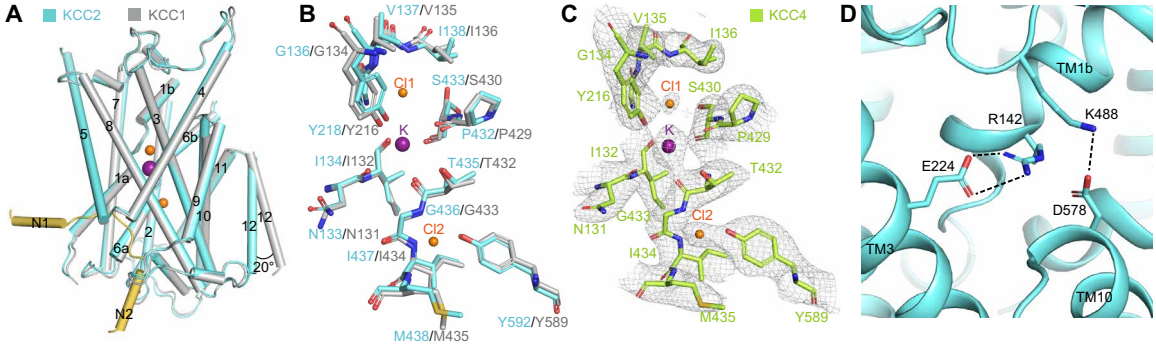

Fig. 2. Structures of the TMD. (**A**) The structural superimposition of KCC2 (cyan) and KCC1 [gray; Protein Data Bank (PDB) 6KKU] at the TMD. In the KCC1 structure, K^+ and Cl^- are shown as purple and orange spheres, respectively. (**B**) K^+ and Cl^- bind at similar positions in KCC2 and KCC1. (**C**) In KCC4 map, the densities of the K^+, Cl^-, and their coordination residues at the contour level of 5σ. (**D**) The extracellular gate of KCC2 is sealed by salt bridges (dash lines).

residues, whereas in KCC1, TM12 is detached and interacts with TM9 from the opposing subunit (*38*).

In the 2.9-Å resolution structure of KCC4, one potassium and two chloride ions are clearly observed (Fig. 2C). These three ions and their coordination residues are identical to those in KCC1. This strict structural conservation between KCCs confirms our previous assignment of ion binding sites in KCC1 (*38*) and is a testament to the importance of preserving their structure to catalyze K-Cl cotransport across the membrane.

KCC2 is in an inward facing conformation, with the extracellular gate occluded by TM7-8 linker and sealed by salt bridges formed between Arg^{142} in TM1b and Glu^{224} in TM3 and between Lys^{488} in TM7-8 linker and Asp^{578} in TM10 (Fig. 2D). As the salt bridges are highly conserved across KCCs and participate in the extracellular gating, mutations in these residues will disrupt the transport cycles and reduce the transport activity, as revealed by the functional studies on KCC3 and KCC4 (*40*, *41*). A mutation of Arg^{207} in human KCC3 (equivalent to Arg^{142} in KCC2) into Cys or His breaks the salt bridge Arg^{207}-Glu^{289} and causes the Andermann syndrome (*42*, *43*).

An autoinhibition state of KCC2

In KCC2, the cytosolic vestibule, formed by TM1a, TM5, TM6b, and TM8, is occupied by an N-terminal peptide covering residues Val^{81} to Asn^{107} (Fig. 3A). The N-terminal peptide inserts into the cavity from the cleft between TM1a and TM5 along the membrane surface, bends by ~110° at Pro^{95}, and goes down toward the CTD (Fig. 3A). This peptide can be divided into three segments, namely two helices N1 (Val^{81} to Asn^{90}) and N2 (Ser^{98} to Asn^{107}) and a linker L12 (Tyr^{91} to Gly^{97}) in between (Fig. 3B and fig. S4B). N1 helix interacts with TM1a and TM5 mainly by hydrophobic interactions (Fig. 3C), whereas L12 establishes an extensive interaction network with TM1a, TM6b, and TM8 by hydrogen bonds. Specifically, Arg^{443} and Arg^{531} tightly hold the peptide as a lock, by forming two strong hydrogen bonds with the carbonyls of Leu^{94} and Pro^{95} (Fig. 3D). The side chain of Gln^{96} also forms two strong hydrogen bonds with the amide groups of Ser^{444} and Gly^{445} (Fig. 3D). N2 helix contains multiple charged or polar residues and interacts with the TMD through hydrogen bonds (Ser^{98}-Arg^{538} and Arg^{99}-Asn^{554}) and the π-π interaction between His^{101} and Tyr^{189} (Fig. 3E). In addition, below N2 helix, the CTD displays a positive electrostatic surface, where the negatively charged residues (Glu102 and Glu105) in N2 helix and a negative electrostatic potential via the helix dipole effect of the N2 helix establish electrostatic interactions with the CTD (Fig. 3F).

To assess the function of the N-terminal peptide, *Xenopus laevis* oocytes were injected with complementary RNA (cRNA) encoding wild-type or mutant KCC2, and the K^+ influx was determined in individual oocyte. As seen in Fig. 3G, a sizable K^+ influx was measured in oocytes injected with wild-type KCC2, compared to that measured in water-injected oocytes. This is consistent with the activity of KCC2 under regular isosmotic conditions. Single amino acid substitution of the conserved residues Tyr^{91}, Thr^{92}, Asn^{93}, Leu^{94}, Gln^{96}, and His^{101} all stimulated the KCC2 function, indicating that the peptide is inhibitory in nature (Fig. 3G). Mutants of the nonconserved residues Ser^{98} and Arg^{99} in N2 helix show lower expression levels, while they maintain similar measured activities to the wild type (fig. S4, A and F). In addition, the substitution of two Glu residues (Glu^{102} + Glu^{105}) in the N2 helix into Ala residues also significantly enhanced the KCC2 function (Fig. 3G). As the two acidic residues contribute to the electrostatic interactions between N2 and CTD, this result suggests that CTD probably stabilizes the autoinhibition state of KCC2.

The N-terminal peptide bound at the cytosolic facing cavity inhibits the function of KCC2 by two ways. First, the N-terminal peptide blocks the intracellular solvent access to the substrate-binding sites in the inward facing conformation (Fig. 3H). Second, the structure comparison of KCC1 in inward- and outward-facing conformations reveals that KCC1 undergoes concerted inward movements of TM8 helix, the intracellular loop between TM6b and TM7, and the short helix between TM2 and TM3 (IL23) when the intracellular gate closes (*44*). In KCC2, the N-terminal peptide forms direct interactions with TM8, IL23, and the TM6b-7 loop and, therefore, constrains their inward movements and locks the transporter in the inward facing state (Fig. 3, D, E, and H). The sequence in the N-terminal peptide, especially in the L12 region, is highly conserved in the KCC family, indicating a common autoinhibition mechanism (fig. S4A). In the KCC4 structure, a similar autoinhibitory peptide is clearly resolved in the cytosolic facing cavity (fig. S4D), while in KCC3, scattered densities are observed in the cytosolic vestibule, suggesting a low occupancy of the N-terminal peptide (fig. S4C).

Dimerization of CTDs

The CTD of KCC2 is an α/β protein and can be further divided into two structurally related subdomains. Each subdomain contains five

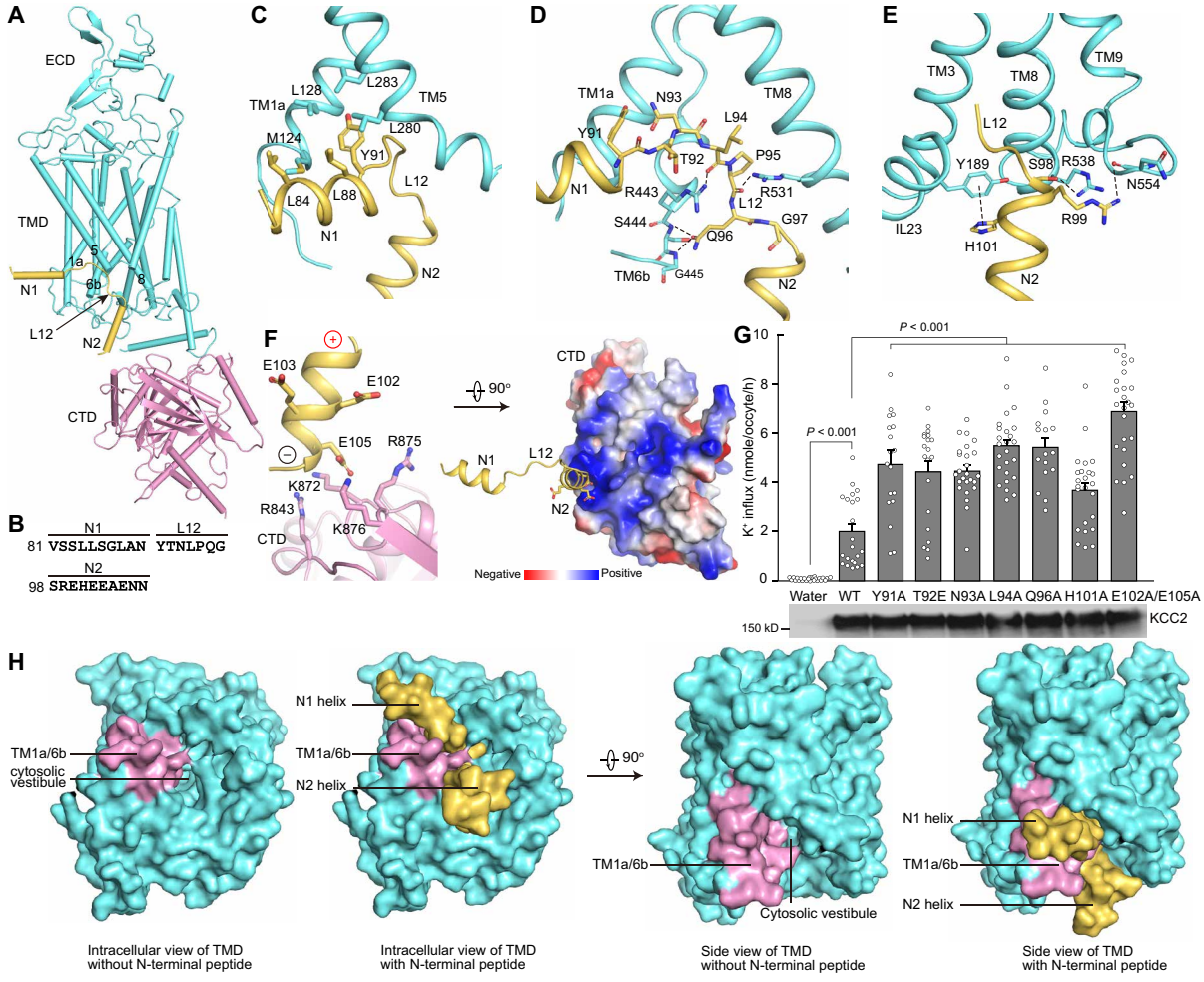

Fig. 3. The N-terminal autoinhibition of KCC2. (**A**) Side view structures of the ECD/TMD (cyan color) and the CTD (pink) from the opposing subunit. The N-terminal peptide is colored in yellow. Numbers show the TM helices lining the cytosolic vestibule. (**B**) Secondary structure assignment of the N-terminal peptide. (**C**) Hydrophobic interactions between N1 and TM1a/TM5. (**D**) Interactions between L12 and TM1a/TM8. Dash lines show hydrogen bonds. (**E**) Interactions between N2 and the TMD. Dash lines show hydrogen bonds or the π-π interaction. (**F**) Electrostatic interactions between N2 and CTD, with CTD shown as cartoon and stick (left) and electrostatic potential surface modes (right). (**G**) K^+ influx in *Xenopus laevis* oocytes injected with wild-type (WT) and mutant KCC2 complementary RNA and measured under isotonic conditions. The Western blot shows that the WT and mutants have similar expression levels. (**H**) The intracellular and the side views of the cytosolic vestibule with or without the N-terminal peptide. The N-terminal peptide is shown as yellow, TM1a and TM6b as pink, and the rest TMD as cyan surface model.

parallel β strands. The 10 β strands form a continuous central β sheet, surrounded by eight α helices (Fig. 4A). In KCC2, a long fragment between β8 and α7 harbors multiple phosphorylation sites and regulates the transporter's activity (*3*). Unfortunately, this fragment was unresolved in the current maps of KCC2. The CTD of KCC2 resembles those of zebrafish NKCC1 (*39*) and the prokaryotic CCC homolog MaCCC (*45*). Compared with KCC2, zebrafish NKCC1 contains two additional helices between β8 and α7 and one between β5 and β6, whereas MaCCC loses α7 (fig. S5, A and B).

The dimerization of CTDs is mainly mediated by hydrophobic interactions, involving the scissor helix, α3-β4 linker, α3 helix, and β3-α3 linker from both subunits (Fig. 4B). First, the two antiparallel scissor helices directly interact with each other by the hydrophobic packing at residues Leu^{673}, Ala^{675}, Ala^{676}, Ala^{679}, and Leu^{683} (Fig. 4C). Second, α3-β4 linkers containing residues ^{786}LGGL^{789} form extensive hydrophobic interactions with the scissor helices (Fig. 4D). Third, a pair of His^{779} residues from α3 helices form π-π interactions (Fig. 4D). Fourth, two hydrogen bonds are formed by Ser^{771} and Asp^{775} in the β3-α3 linker (Fig. 4E). Last, the dimerization of CTDs is further stabilized by the domain-swap organization between the scissor helix and the rest of the CTD (Fig. 4B). The dimerization of KCC2 CTD is similar to that of zebrafish NKCC1 but different from that of MaCCC, which is preserved in solution and in the context of the full-length transporter (fig. S5, C and D) (*45*).

The CTD interacts with the TMD at the junction of TM12 and the scissor helix, where an ~80° turn is formed by the conserved motif ^{665}GDG^{667}. Formed by three hydrogen bonds Lys^{662}-Arg^{694}, Glu^{663}-Gly^{726}, and Asp^{666}-Asn^{692}, the interactions between the CTD and TM12 remain weak (Fig. 4F). In the structures of human NKCC1, KCC1, KCC2C2, and mouse KCC4, CTDs were completely unresolved, probably due to the dissociation of the CTD from the TMD (*37*, *38*, *40*).

Diverse dimerization of the TMD in KCCs

The higher-resolution structures of KCC2, KCC3, and KCC4 have the same dimeric arrangement as zebrafish NKCC1 in the TMD, with the dimer interface formed by TM11 and TM12 (Fig. 5A and

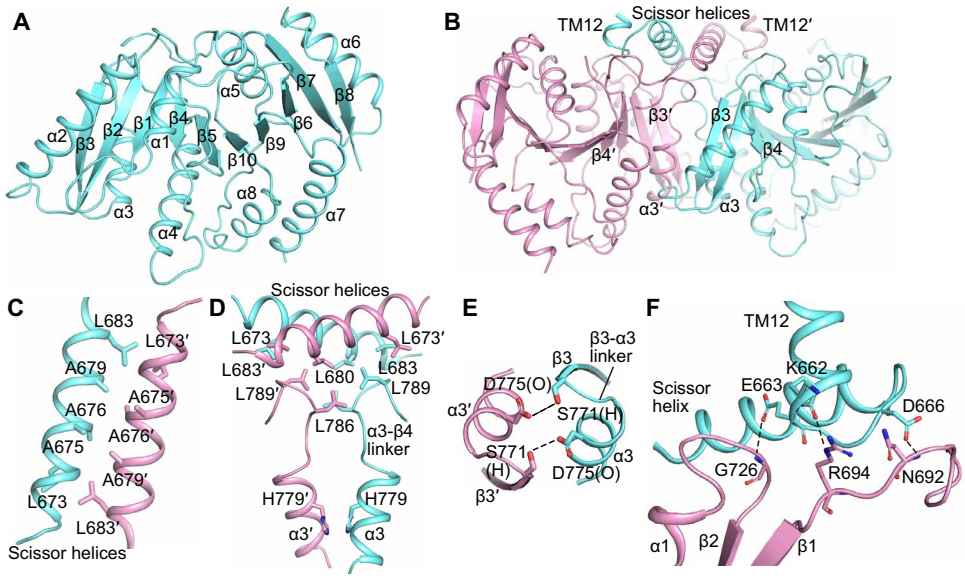

Fig. 4. The dimeric CTD of KCC2. (**A**) The cartoon model of the CTD, with secondary structures labeled. (**B**) The dimeric assembly of CTDs. Two subunits are colored in cyan and pink, individually. The key secondary structure participating in the dimeric organization are labeled. (**C** and **D**) Zoom-in views of the hydrophobic interactions at the dimer interface. (**E**) Hydrogen bonds (dash lines) between β3-α3 linkers from two subunits. The hydrogen bond donor and acceptor groups are labeled. (**F**) Interactions between TM12 and CTD. Dash lines show the hydrogen bonds.

fig. S6A). In KCC2, conserved hydrophobic residues Phe^{634}, Trp^{638}, and Leu^{642} contribute to the dimeric interactions at the junction of TM11 and TM12, below which a large hydrophobic cavity is formed by TM11, TM12, and the TM10 C-terminal end from two subunits (Fig. 5B). In general, the dimeric interactions in the TMD are weak in KCC2 and KCC4 (fig. S6C). In KCC3, the larger distance between two subunits further attenuates the dimeric interactions in the TMD (fig. S6B).

The KCC2C2 structure, although determined at 5.2-Å resolution, clearly represents a different dimeric assembly in the TMD (Fig. 5C and fig. S1). The KCC2C2 dimerization is mediated solely by two almost parallel TM12 helices from two subunits (Fig. 5D). The structural alignment shows no visible conformational difference within one subunit between KCC2 and KCC2C2. The dimeric arrangements of KCC2 and KCC2C2 differ from that of KCC1 dimer, which forms a hydrophobic hole at the dimer interface by hydrophobic interactions between TM12 and TM9 from the opposing subunit (Fig. 5, E and F). When KCC2, KCC2C2, and KCC1 dimers are aligned at one subunit, there are ~90° rotation for the other subunit of KCC2C2 and ~150° rotation for KCC1, relative to that of KCC2 (Fig. 5F). KCC3C2 adopts a similar dimeric assembly as KCC2C2 in the TMD (Fig. 6A and figs. S2 and S6D). In KCC4C2, by contrast, the TMD remains unresolved, while the CTD is of decent quality (figs. S3 and S6E), indicating the relative motions between CTD and TMD. Are these particles of KCC2, KCC3, and KCC4 in class II of any functional significance? The structural rearrangement of KCC3C2 CTD provides clues.

Relative motions between the CTD and the TMD

In the KCC3C2 map, densities connecting CTD and TMD are missing; yet the shape and size of densities at the CTD region allow us to confidently dock the CTD model and reconstruct the full-length transporter (Fig. 6A). To compare the structural difference between KCC3 and KCC3C2, we align two structures at the CTD dimer (Fig. 6B). Around TM12 in each subunit, the TMD of each KCC3C2 subunit undergoes a ~77-Å counterclockwise rotation viewed from the extracellular side, along with a 6- to 7-Å shift away from the CTD, relative to that in KCC3 (Fig. 6B). In the high-resolution structures of KCC2, KCC3, and KCC4, the CTD is positioned just under the TMD, exposing a large area for the TMD to attach (Figs. 1, A to C, and 6C). In particular, the CTD of KCC2 interacts with N2 helix by electrostatic interactions and probably stabilizes the transporter in the autoinhibition state (Fig. 3F). However, in the KCC3C2 structure, the TMD rotates to the right side of the CTD, and the potential interactions between the CTD and N2 helix are eliminated (Fig. 6D). Therefore, structural rearrangement in the TMD may reduce the autoinhibition effect by disrupting interactions between the N-terminal inhibitory peptide and the CTD. The relative position of the CTD to the TMD from the opposing subunit in KCC3C2 resembles that in zebrafish NKCC1 (Fig. 6E) (*39*).

How this relative motion between the CTD and the TMD is induced remains unknown. The linker between TM12 and the scissor helix seems important for the domain organization of the CTD and the TMD. In zebrafish NKCC1, the scissor helix sits at the left side of TM12 (*39*), whereas in KCC2, KCC3, or KCC4, it is at the right side of TM12 (Fig. 6F).

Previously, we determined the dimeric KCC1 structures without visible CTD densities (*38*), and the recently reported structures of human NKCC1 and mouse KCC4 also lost the CTD densities (*37*, *40*). Here, the structures of KCC2C2, KCC3C2, and KCC4C2 provide further evidence to support the view that the mobility of the CTD relative to the TMD is an intrinsic feature of CCCs function. The high-resolution structures of KCC2 and KCC4 provide an autoinhibitory state of KCCs. The scattered densities in the cytosolic facing cavity in KCC3 suggest a mixture of the N-terminal peptide-bound and -unbound states (fig. S4C). In KCC2C2, the densities for L12 and N2 helix in the cytosolic cavity are weakened, indicating a partial dissociation of the inhibitory peptide in the absence of the CTD

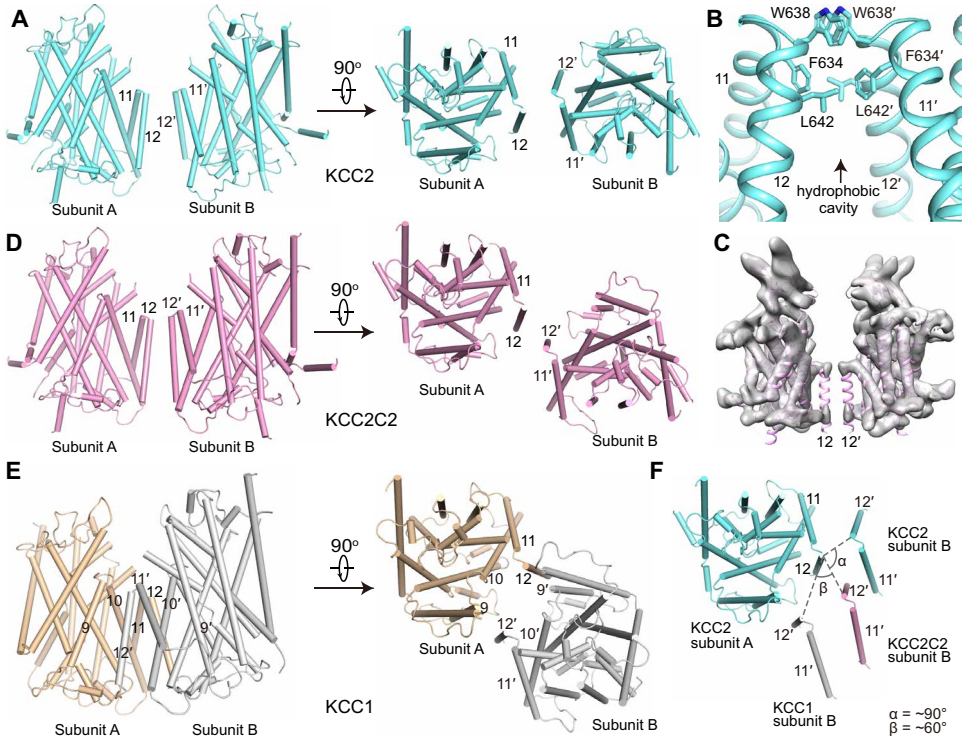

Fig. 5. The dimeric assembly of the TMD. (**A**) The TMD structure of KCC2 dimer. TM11 and TM12 involved in the dimeric assembly are labeled. (**B**) Hydrophobic interactions at the dimer interface of the TMD. Side chains of residues involved in the hydrophobic interactions are shown as stick models. (**C**) Superimposition of the map (gray) and cartoon model (pink) of KCC2C2 dimer. (**D**) The TMD structure of KCC2C2 dimer. (**E**) The TMD structure of KCC1 dimer. Subunit A in KCC2C2 dimer (D) and KCC1 (E) is shown at the same orientation of that in KCC2 dimer (**A**). (**F**) Different dimer interfaces at TMD between KCC2, KCC2C2, and KCC1. Three structures are aligned at the subunit A, and only that of KCC2 is shown. TM11 and TM12 from three subunits B are shown as cartoon models.

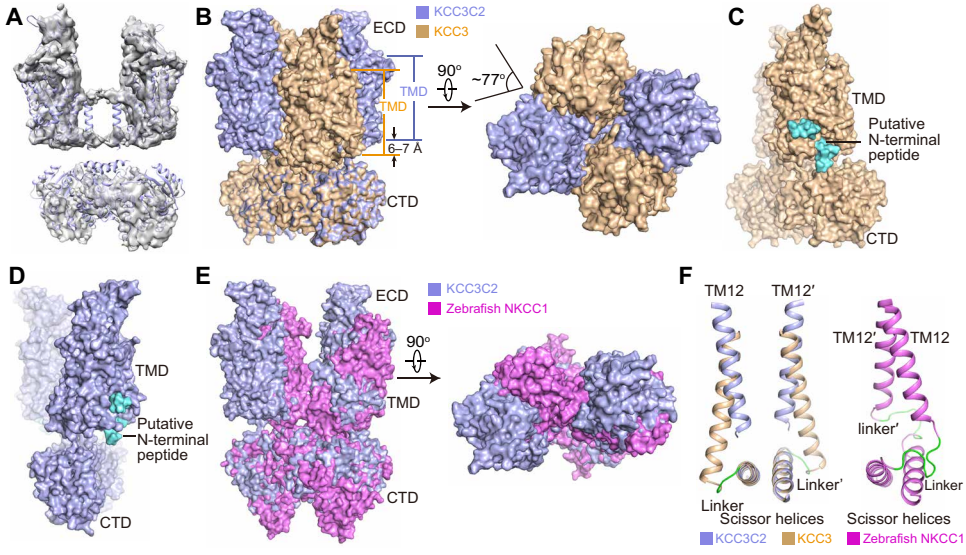

Fig. 6. Motions between the TMD and the CTD of CCCs. (**A**) Superimposition of the map (gray) and cartoon model (blue) of KCC3C2. (**B**) Structural comparisons of KCC3 (light orange) and KCC3C2 (blue) with the CTD dimer aligned. (**C**) In the KCC3 structure (light orange), CTD interacts with the putative N-terminal inhibitory peptide (cyan). (**D**) In the KCC3C2 (blue), after rotation, potential interactions between CTD and the N-terminal inhibitory peptide (cyan) are disrupted. In (**C**) and (**D**), the N-terminal inhibitory peptide is adapted from KCC2 and is shown as cyan surface model. (**E**) Structural comparisons of human KCC3C2 (blue) and zebrafish NKCC1 (magenta) with the CTD dimer aligned. TMDs in NKCC1 are in similar positions as those in KCC3C2, taking into account that the twofold axes of the TMDs and CTDs in NKCC1 do not coincide. (**F**) Structural arrangement of the TM12 and scissor helices in KCC3 (light orange), KCC3C2 (blue), and zebrafish NKCC1 (magenta). The linker between TM12 and scissor helices are colored in green.

(fig. S4E). Similarly, without the CTD, no N-terminal peptide was resolved in the high-resolution structures of human KCC1 dimer and mouse KCC4 monomer (*38*, *40*). KCC3C2 is captured in one specific state with relatively stable TMD and CTD. On the basis of these structures, we propose that the CTD regulates the KCCs' activity by motions relative to the TMD, which affects the binding of the N-terminal inhibitory peptide at the cytosolic facing cavity (fig. S7). The motions may involve the CTD dimer's dissociation, as revealed by these CCC structures without visible CTD and suggested by the FRET assays on NKCC1 (*35*, *36*). Because the dimerization of full-length KCCs is mainly mediated by CTD instead of the TMD, the CTD dimer's dissociation will induce rearrangement of the TMD, which can explain the diverse dimeric assembly of the TMD.

MATERIALS AND METHODS

Protein expression and purification

Human KCC2a, KCC3a, and KCC4a were cloned, expressed, and purified following similar procedures. The human *SLC12A5*, *SLC12A6* and *SLC12A7* genes encoding KCC2a, KCC3a and KCC4a were synthesized (Generalbiol) and cloned into a BacMam expression vector containing an N-terminal FLAG tag and a C-terminal Strep tag II. All three KCCs were heterologously expressed in human embryonic kidney (HEK) 293F cells (Life Technologies) using the BacMam System (Thermo Fisher Scientific). The baculovirus was generated in Sf9 cells (Life Technologies) following the standard protocol and was used to infect HEK293F cells at a ratio of 1: 20 (virus: HEK293F, v:v), supplemented with 10 mM sodium butyrate to boost protein expression.

Cells were cultured in suspension at 37°C for 48 hours and then harvested by centrifugation at 3000*g*. The cell pellet was resuspended in buffer A [30 mM tris-HCl (pH 8.0) and 150 mM KCl] supplemented with a protease inhibitor cocktail (2 μg ml^{-1} deoxyribonuclease I, 2 μg ml^{-1} pepstatin, 2 μg ml^{-1} leupeptin and 2 μg ml^{-1} aprotinin, and 1 mM phenylmethylsulfonyl fluoride) and homogenized by sonication on ice. All three KCCs were extracted with 1% (w:v) lauryl maltose neopentyl glycol (LMNG; Anatrace) supplemented with 0.2% (w:v) cholesteryl hemisuccinate (CHS; Anatrace) by gentle agitation for 2 hours at 4°C. After extraction, the supernatant was collected following a 60-min centrifugation at 48,000*g* and incubated with Anti-DYKDDDDK G1 Affinity Resin (GenScript) with gentle agitation. After 2 hours, the resin was collected on a disposable gravity column (Bio-Rad) and washed in buffer B (buffer A + 0.005% LMNG + 0.02% CHS) for 10-column volumes. The detergent was then changed to 0.02% glyco-diosgenin (GDN), and the protein sample was eluted with FLAG peptide (0.2 mg/ml) in buffer C (buffer A + 0.02% GDN). The protein sample was further purified by size-exclusion chromatography on a Superose 6 10/300 GL column (GE Healthcare) preequilibrated with buffer C. The protein peak fractions were collected and concentrated to appropriate concentrations (6 mg/ml for KCC2, 13 mg/ml for KCC3, and 9 mg/ml for KCC4) for cryo-EM analysis.

EM data acquisition

The cryo-EM grids were prepared by applying 3 μl of KCCs protein to a glow-discharged Quantifoil R1.2/1.3 200/300-mesh copper/gold holey carbon grid (QUANTIFOIL, Micro Tools GmbH, Germany) and blotted for 3.0 s under 100% humidity at 4°C before being plunged into liquid ethane using a Mark IV Vitrobot (FEI). Micrographs were acquired on a Titan Krios microscope (FEI) operated at 300 kV with a K2 Summit direct electron detector (Gatan). SerialEM software was used for automated data collection following the standard procedure. A calibrated magnification of ×49,310 was used for imaging, yielding a pixel size of 1.014 Å on images. The defocus range was set from −1.5 to −2.5 μm. Each micrograph was dose-fractionated to 40 frames under a dose rate of 8 e^-/pixel per second, with a total exposure time of 8 s, resulting in a total dose of about 62 $e^-/Å^2$.

Image processing

The motion correction was performed using the MotionCorr2 program (*46*), and the CTF parameters of the micrographs were estimated using the GCTF program (*47*). All other steps of image processing were performed using RELION 3.0 (*48*).

For KCC2, 2,767,130 particles were automatically picked and extracted from the full data set of 3164 micrographs. The particles were extracted with a binning factor of 3 and were subjected to a 2D classification. A total of 1,888,099 particles were selected for two rounds of 3D classifications using the initial model generated by RELION as the reference. One of the 3D classes showed good secondary structural features, and their particles were selected, combined, and reextracted into the original pixel size of 1.014 Å. After 3D refinement with C2 symmetry and particle polishing with RELION, the resulting 3D reconstruction of KCC2 from 55,026 particles yielded an EM map with a resolution of 3.4 Å (fig. S1). For KCC2C2, the 3D reconstruction from 171,657 particles yielded an EM map with a resolution of 5.2 Å (fig. S1).

For KCC3, 1,819,636 particles were automatically picked and extracted from the full data set of 2090 micrographs. The particles were extracted with a binning factor of 3 and were subjected to a 2D classification. A total of 1,225,521 particles were selected for two rounds of 3D classifications using the model of KCC2 as the reference. One of the 3D classes showed good secondary structural features, and their particles were selected, combined, and reextracted into the original pixel size of 1.014 Å. After 3D refinement with C2 symmetry and particle polishing with RELION, the resulting 3D reconstruction of KCC3 from 84,675 particles yielded an EM map with a resolution of 3.6 Å (fig. S2). For KCC3C2, the 3D reconstruction from 44,936 particles yielded an EM map with a resolution of 7.0 Å (fig. S2).

For KCC4, 1,192,986 particles were automatically picked and extracted from the full data set of 4944 micrographs. The particles were extracted with a binning factor of 3 and were subjected to a 2D classification. A total of 900,777 particles were selected for two rounds of 3D classifications using the model of KCC2 as the reference. One of the 3D classes showed good secondary structural features, and their particles were selected, combined, and reextracted into the original pixel size of 1.014 Å. After 3D refinement with C2 symmetry and particle polishing with RELION, the resulting 3D reconstruction of KCC4 from 95,572 particles yielded an EM map with a resolution of 2.9 Å (fig. S3). For KCC4C2, the 3D reconstruction from 102,049 particles yielded an EM map with a resolution of 7.5 Å (fig. S3).

The resolution was estimated by applying a soft mask around the protein density and the gold-standard Fourier shell correlation (FSC) = 0.143 criterion. Local resolution maps were calculated with RELION (figs. S1 to S3).

Model building, refinement, and validation

De novo atomic model building based on the 3.4-Å resolution density map of KCC2 was performed in Coot (*49*). The KCC2 TMD atomic model building using the KCC1 model as a starting template. The amino acid assignment was achieved on the basis of the clearly defined density for bulky residues (Phe, Trp, Tyr, and Arg). Models were refined against summed maps using phenix.real_space_refine (*50*), with secondary structure restraints and noncrystallography symmetry applied. The initial EM density map allowed us to construct a KCC2 model containing residues 81 to 107, 118 to 916, and 1067 to 1135. The statistics for the models' geometries was generated using MolProbity (*51*) (table S1). All figures were prepared in PyMoL (*52*) or Chimera (*53*).

For KCC3 and KCC4, the atomic model of KCC2 was used as a reference for model building. The final KCC3 model contains residues 183 to 993 and 1078 to 1146, and the KCC4 covers residues 82 to 105, 116 to 913, and 1011 to 1079. For KCC2C2, KCC3C2, and KCC4C2, the models of corresponding TMD and CTD were fitted into low-resolution maps in Chimera.

K^+ (^{83}Rb) influx in oocytes

Fragments of the KCC2 complementary DNA (cDNA) were subcloned into $pBSK^+$ for site-directed mutagenesis (QuikChange from Agilent, Santa Clara, CA). After sequence confirmation of the mutated DNA, fragments were reinserted into the wild-type cDNA to create mutated full-length clones. DNA was then isolated from 60-ml cultures using a mediprep kit from QIAGEN (Valencia, CA) and 2.5 μg purified DNA was linearized with *Mlu*I (New England Biolabs, Beverly, MA). Following the digestion, the DNA was purified using a QIAquick Polymerase Chain Reaction Purification Kit (QIAGEN) and transcribed into cRNA using the mMESSAGE mMACHINE SP6 Transcription Kit (Life Technologies, Grand Island, NY). RNA was then purified by precipitation with LiCl, washed with 70% ethanol, and resuspended in diethylpyrocarbonate–treated water. RNA quality and quantity were then assessed by denaturing agarose gel electrophoresis and spectrophotometric methods.

Extraction of *Xenopus laevis* ovarian lobes was done in accordance with an approved Vanderbilt University Institutional Animal Care and Use Committee protocol and as previously described (*54*). Oocytes were dissociated using collagenase D treatment [4 × 90 min incubation at 4°C in 5 mg collagenase D (Sigma-Aldrich, St. Louis, MO) per ml of a Ca^{2+}-free hypotonic saline (80 mM NaCl instead of 96 mM)].

Oocytes were then maintained overnight in modified L15 solution [250 ml Leibovitz L15 Ringer (Invitrogen, Carlsbad, CA), 200-ml deionized water, 952 mg Hepes (acid form), and 44 M gentamycin (Invitrogen; pH 7.4); 195 to 200 mosM] at 16°C. The following day, groups of 25 to 30 oocytes were injected with 50-nl water containing 15 ng KCC2 cRNA and incubated for 3 days at 16°C. Medium was replaced the day following the injection. KCC2 function was assessed 3 days postinjection.

We used *Xenopus laevis* oocytes for our functional studies because they are large cells with minimal K^+ uptake mechanisms. Thus, most of the signal obtained from the oocytes originates from the heterologous expression of the transporters injected. To further ensure low background, we perform the K^+ uptake measurements in a Na^+-free solution to eliminate the participation of the endogenous Na-K-2Cl cotransporter and, in the presence of ouabain, to eliminate Na^+/K^+ pump activity. Thus, K^+ influx is measured in a solution containing 96 mM N-methyl-D-glucamine-Cl, 4 mM KCl, 1 mM $CaCl_2$, 0.8 mM $MgSO_4$, 5 mM Hepes, and 100 mM ouabain (pH 7.4). The osmolarity of the solution is 200 mOsM to match the frog internal milieu. KCC2 activity is assessed through K^+ influx, which is calculated from unidirectional radioisotope tracer uptake. Groups of 20 to 25 oocytes are rinsed once with 3 ml Na^+-free solution without ouabain, preincubated for 15 min in 1 ml of same solution containing ouabain, and then fluxed for 1 hour in 1 ml of identical solution containing 2.5 μCi/ml radioactive Rb^+ as a tracer for K^+ movement. As ^{86}Rb is no longer commercially available, we purchased ^{83}Rb from the Brookhaven radioisotope production facility. The isotope has a longer half-life (86.2 versus 18.6 days for ^{86}Rb) and has emission energies that can be detected by either gamma detector (at 520 keV) or liquid scintillation counting (window set to energies of 0 to 100 keV). K^+ influx is calculated from the amount of ^{83}Rb that has entered each oocyte over a period of 1 hour and is expressed in nmol K^+ $oocyte^{-1}$ $hour^{-1}$. All data points are means ± SEM ($n \geq 15$). The one-way analysis of variance (ANOVA) was used to determine whether there are any statistically significant differences between the means of wild-type KCC2 and mutants.

For Western blot analysis, groups of eight oocytes were homogenized with pipet in 240-μl lysis buffer containing 150 mM NaCl, 50 mM tris (pH 8.5), 2 mM EDTA, 0.1% SDS, 0.5% Na-12 deoxycholate, and 1% CHAPS and incubated on ice for 30 min. The samples were then spun at maximum speed at 4°C for 20 min, and the supernatant was collected and passed through a spin column to eliminate any residual yolk. Samples (40 μl) were added to 40-μl 4× sample buffer + dithiothreitol and denatured at 70°C for 15 min. After separation on 7.5% polyacrylamide gel, proteins were transferred to polyvinylidene difluoride membrane, which was incubated overnight with anti–c-Myc antibody (mouse monoclonal, clone 9E10 from Thermo Fisher Scientific).

SUPPLEMENTARY MATERIALS

Supplementary material for this article is available at http://advances.sciencemag.org/cgi/content/full/6/50/eabc5883/DC1

View/request a protocol for this paper from *Bio-protocol*.

REFERENCES AND NOTES

1. G. Gamba, Molecular physiology and pathophysiology of electroneutral cation-chloride cotransporters. *Physiol. Rev.* **85**, 423–493 (2005).
2. S. C. Hebert, D. B. Mount, G. Gamba, Molecular physiology of cation-coupled Cl^- cotransport: The SLC12 family. *Pflugers Arch.* **447**, 580–593 (2004).
3. J. P. Arroyo, K. T. Kahle, G. Gamba, The SLC12 family of electroneutral cation-coupled chloride cotransporters. *Mol. Aspects Med.* **34**, 288–298 (2013).
4. J. M. Russell, Sodium-potassium-chloride cotransport. *Physiol. Rev.* **80**, 211–276 (2000).
5. N. Obermüller, P. Bernstein, H. Velázquez, R. Reilly, D. Moser, D. H. Ellison, S. Bachmann, Expression of the thiazide-sensitive Na-Cl cotransporter in rat and human kidney. *Am. J. Physiol.* **269**, F900–F910 (1995).
6. T. Fujii, Y. Takahashi, A. Ikari, M. Morii, Y. Tabuchi, K. Tsukada, N. Takeguchi, H. Sakai, Functional association between K^+-Cl^- cotransporter-4 and H^+,K^+-ATPase in the apical canalicular membrane of gastric parietal cells. *J. Biol. Chem.* **284**, 619–629 (2008).
7. T. Fujii, Y. Takahashi, Y. Itomi, K. Fujita, M. Morii, Y. Tabuchi, S. Asano, K. Tsukada, N. Takeguchi, H. Sakai, K^+-Cl^-cotransporter-3a up-regulates Na^+,K^+-ATPase in lipid rafts of gastric luminal parietal cells. *J. Biol. Chem.* **283**, 6869–6877 (2008).
8. E. Delpire, K. B. Gagnon, Na^+-K^+-$2Cl^-$ Cotransporter (NKCC) physiological function in nonpolarized cells and transporting epithelia. *Compr. Physiol.* **8**, 871–901 (2018).
9. M. Becker, H. G. Nothwang, E. Friauf, Differential expression pattern of chloride transporters *NCC, NKCC2, KCC1, KCC3, KCC4*, and *AE3* in the developing rat auditory brainstem. *Cell Tissue Res.* **312**, 155–165 (2003).
10. P. K. Lauf, J. Zhang, E. Delpire, R. E. W. Fyffe, D. B. Mount, N. C. Adragna, K-Cl co-transport: Immunocytochemical and functional evidence for more than one KCC isoform in high K and low K sheep erythrocytes. *Comp. Biochem. Physiol. A Mol. Integr. Physiol.* **130**, 499–509 (2001).

11. E. Delpire, K. B. Gagnon, Water homeostasis and cell volume maintenance and regulation. *Curr. Top Membr.* **81**, 3–52 (2018).
12. C. A. Hübner, V. Stein, I. Hermans-Borgmeyer, T. Meryer, K. Ballanyi, T. J. Jentsch, Disruption of KCC2 reveals an essential role of K-Cl cotransport already in early synaptic inhibition. *Neuron* **30**, 515–524 (2001).
13. C. Rivera, J. Voipio, J. A. Payne, E. Ruusuvuori, H. Lahtinen, K. Lamsa, U. Pirvola, M. Saarma, K. Kaila, The K^+/Cl^- co-transporter KCC2 renders GABA hyperpolarizing during neuronal maturation. *Nature* **397**, 251–255 (1999).
14. D. B. Simon, C. Nelson-Williams, M. Johnson Bia, D. Ellison, F. E. Karet, A. Morey Molina, I. Vaara, F. Iwata, H. M. Cushner, M. Koolen, F. J. Gainza, H. J. Gitelman, R. P. Lifton, Gitelman's variant of Bartter's syndrome, inherited hypokalaemic alkalosis, is caused by mutations in the thiazide-sensitive Na–Cl cotransporter. *Nat. Genet.* **12**, 24–30 (1996).
15. D. B. Simon, F. E. Karet, J. M. Hamdan, A. D. Pietro, S. A. Sanjad, R. P. Lifton, Bartter's syndrome, hypokalaemic alkalosis with hypercalciuria, is caused by mutations in the Na–K–2Cl cotransporter *NKCC2*. *Nat. Genet.* **13**, 183–188 (1996).
16. H. C. Howard, D. B. Mount, D. Rochefort, N. Byun, N. Dupré, J. Lu, X. Fan, L. Song, J.-B. Rivière, C. Prévost, J. Horst, A. Simonati, B. Lemcke, R. Welch, R. England, F. Q. Zhan, A. Mercado, W. B. Siesser, A. L. George Jr., M. P. McDonald, J.-P. Bouchard, J. Mathieu, E. Delpire, G. A. Rouleau, The K–Cl cotransporter KCC3 is mutant in a severe peripheral neuropathy associated with agenesis of the corpus callosum. *Nat. Genet.* **32**, 384–392 (2002).
17. K. T. Kahle, N. D. Merner, P. Friedel, L. Silayeva, B. Liang, A. Khanna, Y. Shang, P. Lachance-Touchette, C. Bourassa, A. Levert, P. A. Dion, B. Walcott, D. Spiegelman, A. Dionne-Laporte, A. Hodgkinson, P. Awadalla, H. Nikbakht, J. Majewski, P. Cossette, T. Z. Deeb, S. J. Moss, I. Medina, G. A. Rouleau, Genetically encoded impairment of neuronal KCC2 cotransporter function in human idiopathic generalized epilepsy. *EMBO Rep.* **15**, 766–774 (2014).
18. T. Saito, A. Ishii, K. Sugai, M. Sasaki, S. Hirose, A de novo missense mutation in *SLC12A5* found in a compound heterozygote patient with epilepsy of infancy with migrating focal seizures. *Clin. Genet.* **92**, 654–658 (2017).
19. T. Stödberg, A. M. Tague, A. J. Ruiz, H. Hirata, J. Zhen, P. Long, I. Farabella, E. Meyer, A. Kawahara, G. Vassallo, S. M. Stivaros, M. K. Bjursell, H. Stranneheim, S. Tigerschiöld, B. Persson, I. Bangash, K. Das, D. Hughes, N. Lesko, J. Lundeberg, R. C. Scott, A. Poduri, I. E. Scheffer, H. Smith, P. Gissen, S. Schorge, M. E. A. Reith, M. Topf, D. M. Kullmann, R. J. Harvey, A. Wedell, M. A. Kurian, Mutations in *SLC12A5* in epilepsy of infancy with migrating focal seizures. *Nat. Commun.* **6**, 8038 (2015).
20. S. N. Orlov, S. V. Koltsova, L. V. Kapilevich, N. O. Dulin, S. V. Gusakova, Cation-chloride cotransporters: regulation, physiological significance, and role in pathogenesis of arterial hypertension. *Biochemistry* **79**, 1546–1561 (2014).
21. T.-Y. Chun, L. Bankir, G. J. Eckert, D. G. Bichet, C. Saha, S.-A. Zaidi, M. A. Wagner, J. H. Pratt, Ethnic differences in renal responses to furosemide. *Hypertension* **52**, 241–248 (2008).
22. E. Delpire, A. Baranczak, A. G. Waterson, K. Kim, N. Kett, R. D. Morrison, J. Scott Daniels, C. David Weaver, C. W. Lindsley, Further optimization of the K-Cl cotransporter KCC2 antagonist ML077: Development of a highly selective and more potent in vitro probe. *Bioorg. Med. Chem. Lett.* **22**, 4532–4535 (2012).
23. E. Delpire, E. Days, L. M. Lewis, D. Mi, K. Kim, C. W. Lindsley, C. D. Weaver, Small-molecule screen identifies inhibitors of the neuronal K-Cl cotransporter KCC2. *Proc. Natl. Acad. Sci. U.S.A.* **106**, 5383–5388 (2009).
24. F. Ferrini, L. E. Lorenzo, A. G. Godin, M. L. Quang, Y. De Koninck, Enhancing KCC2 function counteracts morphine-induced hyperalgesia. *Sci. Rep.* **7**, 3870 (2017).
25. P. N. Lizhnyak, P. P. Muldoon, P. P. Pilaka, J. T. Povlishock, A. K. Ottens, Traumatic brain injury temporal proteome guides KCC2-Targeted Therapy. *J. Neurotrauma* **36**, 3092–3102 (2019).
26. M. Gagnon, M. J. Bergeron, G. Lavertu, A. Castonguay, S. Tripathy, R. P. Bonin, J. Perez-Sanchez, D. Boudreau, B. Wang, L. Dumas, I. Valade, K. Bachand, M. Jacob-Wagner, C. Tardif, I. Kianicka, P. Isenring, G. Attardo, J. A. M. Coull, Y. de Koninck, Chloride extrusion enhancers as novel therapeutics for neurological diseases. *Nat. Med.* **19**, 1524–1528 (2013).
27. Y. G. Shi, Common folds and transport mechanisms of secondary active transporters. *Annu. Rev. Biophys.* **42**, 51–72 (2013).
28. A.-M. Hartmann, H. G. Nothwang, Molecular and evolutionary insights into the structural organization of cation chloride cotransporters. *Front. Cell. Neurosci.* **8**, 470 (2015).
29. J. A. Payne, Molecular operation of the cation chloride cotransporters: Ion binding and inhibitor interaction. *Curr. Top Membr.* **70**, 215–237 (2012).
30. J. Ding, J. Ponce-Coria, E. Delpire, A trafficking-deficient mutant of KCC3 reveals dominant-negative effects on K-Cl cotransport function. *PLOS ONE* **8**, e61112 (2013).
31. H. H. Lee, R. Jurd, S. J. Moss, Tyrosine phosphorylation regulates the membrane trafficking of the potassium chloride co-transporter KCC2. *Mol. Cell. Neurosci.* **45**, 173–179 (2010).
32. H. H. Lee, J. A. Walker, J. R. Williams, R. J. Goodier, J. A. Payne, S. J. Moss, Direct protein kinase C-dependent phosphorylation regulates the cell surface stability and activity of the potassium chloride cotransporter KCC2. *J. Biol. Chem.* **282**, 29777–29784 (2007).
33. M. V. Sorensen, S. Grossmann, M. Roesinger, N. Gresko, A. P. Todkar, G. Barmettler, U. Ziegler, A. Odermatt, D. Loffing-Cueni, J. Loffing, Rapid dephosphorylation of the renal sodium chloride cotransporter in response to oral potassium intake in mice. *Kidney Int.* **83**, 811–824 (2013).
34. K. Strange, T. D. Singer, R. Morrison, E. Delpire, Dependence of KCC2 K-Cl cotransporter activity on a conserved carboxy terminus tyrosine residue. *Am. J. Physiol. Cell Physiol.* **279**, C860–C867 (2000).
35. M. Pedersen, M. Carmosino, B. Forbush, Intramolecular and intermolecular fluorescence resonance energy transfer in fluorescent protein-tagged na-k-cl cotransporter (NKCC1): Sensitivity to regulatory conformational change and cell volume. *J. Biol. Chem.* **283**, 2663–2674 (2008).
36. M. Y. Monette, B. Forbush, Regulatory activation is accompanied by movements in the C-terminus of the Na-K-Cl cotransporter (NKCC1). *J. Biol. Chem.* **26**, 2210–2220 (2012).
37. X. Yang, Q. Wang, E. Cao, Structure of the human cation–chloride cotransporter NKCC1 determined by single-particle electron cryo-microscopy. *Nat. Commun.* **11**, 1016 (2020).
38. S. Liu, S. Chang, B. Han, L. Xu, M. Zhang, C. Zhao, W. Yang, F. Wang, J. Li, E. Delpire, S. Ye, X.-C. Bai, J. Guo, Cryo-EM structures of the human cation-chloride cotransporter KCC1. *Science* **366**, 505–508 (2019).
39. T. A. Chew, B. J. Orlando, J. Zhang, N. R. Latorraca, A. Wang, S. A. Hollingsworth, D. H. Chen, R. O. Dror, M. Liao, L. Feng, Structure and mechanism of the cation–chloride cotransporter NKCC1. *Nature* **572**, 488–492 (2019).
40. M. S. Reid, D. M. Kern, S. G. Brohawn, Cryo-EM structure of the potassium-chloride cotransporter KCC4 in lipid nanodiscs. *eLife* **9**, e52505 (2020).
41. A. Salin-Cantegrel, J.-B. Rivière, M. Shekarabi, S. Rasheed, S. DaCal, J. Laganière, R. Gaudet, D. Rochefort, G. Lesca, C. Gaspar, P. A. Dion, J.-Y. Lapointe, G. A. Rouleau, Transit defect of potassium-chloride Co-transporter 3 is a major pathogenic mechanism in hereditary motor and sensory neuropathy with agenesis of the corpus callosum. *J. Biol. Chem.* **286**, 28456–28465 (2011).
42. G. Uyanik, N. Elcioglu, J. Penzien, C. Gross, Y. Yilmaz, A. Olmez, E. Demir, D. Wahl, K. Scheglmann, B. Winner, U. Bogdahn, H. Topaloglu, U. Hehr, J. Winkler, Novel truncating and missense mutations of the *KCC3* gene associated with Andermann syndrome. *Neurology* **66**, 1044–1048 (2006).
43. J. Park, B. R. Flores, K. Scherer, H. Kuepper, M. Rossi, K. Rupprich, M. Rautenberg, N. Deininger, A. Weichselbaum, A. Grimm, M. Sturm, U. Grasshoff, E. Delpire, T. B. Haack, *De novo* variants in *SLC12A6* cause sporadic early-onset progressive sensorimotor neuropathy. *J. Med. Genet.* **57**, 283–288 (2020).
44. Y. Zhao, J. Shen, Q. Wang, M. Zhou, E. Cao, Inhibitory and transport mechanisms of the human cation–chloride cotransport KCC1. 10.1101/2020.07.26.221770 (2020).
45. S. Warmuth, I. Zimmermann, R. Dutzler, X-ray structure of the C-terminal domain of a prokaryotic cation–chloride cotransporter. *Structure* **17**, 538–546 (2009).
46. S. Q. Zheng, E. Palovcak, J. P. Armache, K. A. Verba, Y. Cheng, D. A. Agard, MotionCor2: Anisotropic correction of beam-induced motion for improved cryo-electron microscopy. *Nat. Methods* **14**, 331–332 (2017).
47. K. Zhang, Gctf: Real–time CTF determination and correction. *J. Struct. Biol.* **193**, 1–12 (2016).
48. S. H. Scheres, RELION: Implementation of a Bayesian approach to cryo-EM structure determination. *J. Struct. Biol.* **180**, 519–530 (2012).
49. P. Emsley, B. Lohkamp, W. G. Scott, K. Cowtan, Features and development of *Coot*. *Acta Crystallogr. D Biol. Crystallogr.* **66**, 486–501 (2010).
50. P. D. Adams, P. V. Afonine, G. Bunkóczi, V. B. Chen, I. W. Davis, N. Echols, J. J. Headd, L.-W. Hung, G. J. Kapral, R. W. Grosse-Kunstleve, A. J. McCoy, N. W. Moriarty, R. Oeffner, R. J. Read, D. C. Richardson, J. S. Richardson, T. C. Terwilliger, P. H. Zwart, *PHENIX*: A comprehensive Python-based system for macromolecular structure solution. *Acta Crystallogr. D Biol. Crystallogr.* **66**, 213–221 (2010).
51. V. B. Chen, W. B. Arendall III, J. J. Headd, D. A. Keedy, R. M. Immormino, G. J. Kapral, L. W. Murray, J. S. Richardson, D. C. Richardson, *MolProbity*: All-atom structure validation for macromolecular crystallography. *Acta Crystallogr. D Biol. Crystallogr.* **66**, 12–21 (2010).
52. L. Schrödinger, The PyMOL Molecular Graphics System, Version 1.8 (2015).
53. E. F. Pettersen, T. D. Goddard, C. C. Huang, G. S. Couch, D. M. Greenblatt, E. C. Meng, T. E. Ferrin, UCSF Chimera—A visualization system for exploratory research and analysis. *J. Comput. Chem.* **25**, 1605–1612 (2004).
54. K. B. E. Gagnon, R. England, E. Delpire, Volume sensitivity of cation-Cl^- cotransporters is modulated by the interaction of two kinases: Ste20-related proline-alanine-rich kinase and WNK4. *Am. J. Physiol. Cell Physiol.* **290**, C134–C142 (2006).

Acknowledgments: Single particle cryo-EM data were collected at Center of Cryo-Electron Microscopy at Zhejiang University. We thank X. Zhang for support in facility access and data acquisition. **Funding:** This work was supported in part by Ministry of Science and Technology (2020YFA090023 to J.G. and S.Y., 2018YFA0508100 to J.G., and 2016YFA0500404 to S.Y.), the National Natural Science Foundation of China (31870724 to J.G.; 31525001 and 31430019 to

S.Y), Zhejiang Provincial Natural Science Foundation (LR19C050002 to J.G.), and the Fundamental Research Funds for the Central Universities (to J.G. and S.Y.). S.C. is supported by grants from Laboratory and equipment management, Zhejiang University (SJS201814). E.D. is supported by NIH grants DK093501, DK110375, and by Leducq Foundation grant 17CVD05.
Author Contributions: J.G. and S.Y. conceived and designed this project. Y.X., C.Z., F.W., S.L., and J.W. prepared the samples. Y.X., S.C., J.G., and S.Y. performed data acquisition, image processing, and structure determination. E.D. performed the K^+ influx assay. All authors participated in the data analysis and manuscript preparation. **Competing interests:** The authors declare that they have no competing interests. **Data and materials availability:** Cryo-EM density maps have been deposited in the Electron Microscopy Data Bank (EMDB) under accession numbers EMD-30615 for KCC2, EMD-30616 for KCC3, and EMD-30617 for KCC4. Structure coordinates have been deposited in the protein data bank (PDB) under accession numbers 7D8Z for KCC2, 7D90 for KCC3, and 7D99 for KCC4.

Submitted 2 May 2020
Accepted 21 October 2020
Published 11 December 2020
10.1126/sciadv.abc5883

Citation: Y. Xie, S. Chang, C. Zhao, F. Wang, S. Liu, J. Wang, E. Delpire, S. Ye, J. Guo, Structures and an activation mechanism of human potassium-chloride cotransporters. *Sci. Adv.* **6**, eabc5883 (2020).